Disentangling the Cosmic Web I: Morphology of Isodensity Contours

Jens Schmalzing[1,2,*], Thomas Buchert[3,1,†], Adrian L. Melott[4,‡], Varun Sahni[5,§], B. S. Sathyaprakash[6,¶], and Sergei F. Shandarin[4,7,‖]

ABSTRACT

We apply Minkowski functionals and various derived measures to decipher the morphological properties of large–scale structure seen in simulations of gravitational evolution. Minkowski functionals of isodensity contours serve as tools to test global properties of the density field. Furthermore, we identify coherent objects at various threshold levels and calculate their partial Minkowski functionals. We propose a set of two derived dimensionless quantities, planarity and filamentarity, which reduce the morphological information in a simple and intuitive way. Several simulations of the gravitational evolution of initial power–law spectra provide a framework for systematic tests of our method.

Subject headings: methods: numerical; methods: statistical; dark matter; large-scale structure of Universe

---

[1]Ludwig–Maximilians–Universität, Theresienstraße 37, 80333 München, Germany.

[2]Max–Planck–Institut für Astrophysik, Karl–Schwarzschild–Straße 1, 85740 Garching, Germany.

[3]Theory Division, CERN, 1211 Genève 23, Switzerland.

[4]Department of Physics and Astronomy, University of Kansas, Lawrence, Kansas 66045, USA.

[5]Inter–University Centre for Astronomy and Astrophysics, Post Bag 4, Pune 411007, India.

[6]Department of Physics and Astronomy, University of Wales, College of Cardiff, Cardiff CF2 3YB, UK.

[7]Theoretical Astrophysics Center, Juliane Maries Vej 30, 2100 Køpnhavn Ø, Denmark.

[*]email jensen@mpa-garching.mpg.de

[†]email buchert@theorie.physik.uni-muenchen.de

[‡]email melott@kusmos.phsx.ukans.edu

[§]email varun@iucaa.ernet.in

[¶]email spxbss@astro.cf.ac.uk

[‖]email sergei@kusmos.phsx.ukans.edu

1. Introduction

The existence of the large–scale clustering of galaxies had already been well established by the early 1970's mainly due to the pioneering work of Totsuji & Kihara (1969) and Peebles (1974) who showed that the two–point correlation function for galaxies in the Lick and Zwicky catalogues was positive and had the power-law form $\xi(r) \propto r^{-1.8}$ on scales $\lesssim 10h^{-1}$Mpc. Their result was later extended to three–dimensional galaxy catalogues as well. Although the clustering of galaxies is now a well–known fact, a complete description of clustering which includes its geometrical features has so far eluded researchers. This is perhaps due to the fact that the galaxy density field which we observe appears to be strongly non–Gaussian. A Gaussian random field is uniquely described by its power spectrum $P(k)$, or its two–point correlation function $\xi(r)$ since $\xi(r)$ and $P(k)$ form a Fourier transform pair. This is no longer true for a non–Gaussian field for which ξ must be complemented by other statistical descriptors which are sensitive to the structure of matter on large scales. In the so-called "standard model" of structure formation, an initially Gaussian density distribution becomes non–Gaussian due to mode-coupling and the resultant build up of phase correlations during the non–linear regime. These phase correlations give rise to the amazing diversity of form, which is characteristic of a highly evolved distribution of matter, and is often referred to as being cellular, filamentary, sheet–like, network–like, sponge–like, a cosmic web etc. Most of these descriptions are based either on a visual appearance of large–scale structure or on the presence of features that are absent in the reference Gaussian distribution which, by definition, is assumed to be featureless. Gravitational instability, for example, may cause CDM–like Gaussian initial perturbations to evolve towards a density field that percolates at a higher density threshold, i.e. at a lower filling factor, than a Gaussian field (Melott et al. 1983). Such distributions display greater connectivity and are sometimes referred to as being "network–like" (Yess & Shandarin 1996).

In order to come to grips with the rich textural possibilities inherent in large–scale structure, a number of geometrical indicators of clustering have been proposed in the past including minimal spanning trees (Barrow et al. 1985), the genus curve (Gott III et al. 1986), percolation theory (Zel'dovich & Shandarin 1982; Shandarin 1983) and shape analysis (Sathyaprakash et al. 1998; Sahni & Coles 1995 and references therein). A major recent advance in our understanding of gravitational clustering has been associated with the application of Minkowski functionals (MFs) to cosmology (Mecke et al. 1994). The four MFs $V_0, \ldots, V_3$ provide an excellent description of the geometrical properties of a collection of point objects (galaxies) or, alternatively, of continuous distributions such as density fields in large–scale structure or brightness contours in the cosmic microwave background. The scope and descriptive power of the MFs is enhanced by the fact that both percolation analysis and the genus curve are members of the family. Additionally, as demonstrated by Sahni et

al. (1998), ratios of MFs provide us with an excellent "shape statistic" with which one may attempt to quantify the morphology of large scale structure, including the shapes of individual superclusters and voids. Spurred by the success of MFs in quantifying the geometrical properties of large–scale structure we apply the MFs to scale–invariant N–body simulations of gravitational clustering, with an attempt to probe both the global properties and the individual "bits and pieces" that might make up the "cosmic web" (Bond et al. 1996).

2. Method

2.1. Minkowski functionals

Minkowski functionals (named after Minkowski 1903) were introduced into cosmology by Mecke et al. (1994) employing the generalized Boolean grain model. This model associates a body with a point process (in our case given by the location of galaxies or clusters) by decorating each point with a ball of radius r. The union set of the covering balls is then studied morphologically, whereby the radius of the ball serves as a diagnostic parameter probing the spatial scale of the body.

In this paper we shall use the excursion set approach which is applicable to continuous fields (that may be constructed from point processes). Schmalzing & Buchert (1997) pointed out how to apply Minkowski functionals to isocontours of continuous fields, where the contour level (the threshold) is employed as diagnostic parameter. The excursion set approach inherits two diagnostic parameters, because we may also vary the smoothing scale used in constructing the continuous field.

In three dimensions there exist four Minkowski functionals V_μ, $\mu = 0, 1, 2, 3$. They provide a complete and unique description of a pattern's global morphology in the sense of Hadwiger's theorem (Hadwiger 1957). While reducing the information contained in the full hierarchy of correlation functions, this small set of numbers incorporates correlations of arbitrary order and therefore provides a complementary look on large–scale structure. The geometric interpretations of all Minkowski functionals in three dimensions are summarized in Table 1.

We calculate global Minkowski functionals of the isodensity contours of the density field as described in Appendix A. Furthermore, we separately calculate the partial Minkowski functionals of each isolated part of the isodensity contour. Since the total isodensity contour is the union of all its parts, the global functionals are given as sums of the partial functionals at the same threshold. This follows the spirit of Mecke et al. (1994), where partial Minkowski functionals are introduced to measure local morphology for the generalized Boolean grain

model.

Partial Minkowski functionals (PMF) offer the possibility of probing the morphology of individual objects, or the object's environmental morphological properties, respectively. We expect that this concept will be more powerful when applied to continuous fields at high spatial resolution so that the details of structures are not smoothed out. Their application to point processes also delivers more direct information. PMF provide a wide range of possibilities for morphological studies which we shall explore in a forthcoming paper.

2.2. Shapefinders

One important task of morphological statistics consists in quantifying strongly non–Gaussian features such as filaments and pancakes. Given the four Minkowski functionals, we aim at reducing their morphological information content to two measures of planarity and filamentarity, respectively, as has been done for example with various geometrical quantities (Mo & Buchert 1990), moments of inertia (Babul & Starkman 1992), and cumulants of counts–in–cells (Luo & Vishniac 1995).

Recently, Sahni et al. (1998) proposed a set of shapefinders derived from Minkowski functionals. One starts from the three independent ratios of Minkowski functionals that have dimension of length. Requiring that they yield the radius R if applied to a ball, we define

$$\text{Thickness } T := \frac{V_0}{2V_1}, \qquad \text{Width } W := \frac{2V_1}{\pi V_2}, \qquad \text{Length } L := \frac{3V_2}{4V_3}. \tag{1}$$

By the isoperimetric inequalities (B5), we have $L \geq W \geq T$ for any convex body.

Going one step further, Sahni et al. (1998) also define dimensionless shapefinders by

$$\text{Planarity } \mathcal{P} := \frac{W-T}{W+T}, \qquad \text{Filamentarity } \mathcal{F} := \frac{L-W}{L+W}. \tag{2}$$

Some examples are in order.

2.3. Simple examples

Let us consider some simple families of convex bodies in three–dimensional space that can take both filamentary and planar shape.

A spheroid with two axes of length r and one axis of length λr has Minkowski functionals

$$V_0 = \frac{4\pi}{3} r^3 \lambda, \qquad V_1 = \frac{\pi}{3} r^2 \left(1 + f(1/\lambda)\right), \qquad V_2 = \frac{2}{3} r \left(\lambda + f(\lambda)\right), \qquad V_3 = 1, \tag{3}$$

where[6]

$$f(x) = \frac{\arccos x}{\sqrt{1 - x^2}}. \tag{4}$$

By varying the parameter λ from zero to infinity, we can change the morphology of the spheroid from a filament to a pancake via a spherical cluster.

A different way of deforming a filament into a pancake goes via generic triaxial ellipsoids; thereby one of the smaller axes of a strongly prolate spheroid is increased in size until it matches the larger axis and an oblate spheroid has been reached. An integral expression can be found in (Sahni et al. 1998).

Yet another transition from prolate to oblate shape is provided by cylinders of radius r and height λr. Here, the Minkowski functionals are given by

$$V_0 = \pi r^3 \lambda, \qquad V_1 = \frac{\pi}{3} r^2 (1 + \lambda), \qquad V_2 = \frac{1}{3} r (\pi + \lambda), \qquad V_3 = 1. \tag{5}$$

A Blaschke diagram, that is a plot of planarity $\mathcal{P}$ and filamentarity $\mathcal{F}$, summarizing the morphological properties of these simple convex bodies is shown in Figure 1.

3. A set of N–body simulations

3.1. Description

We start from a family of initial power law spectra $P(k) \propto k^n$ with $n \in \{-2, -1, 0, +1\}$ set before an Einstein–de Sitter background (Ω=1, Λ=0). We conduct numerical experiments using a PM code (consult Melott & Shandarin 1993 for details). Four sets of phases were used for each model, making a total of 16 simulation runs. Each run consists of 128^3 particles sampled at an epoch well in the non–linear regime. This epoch is chosen such that the scale of non–linearity $k_{\rm nl}$, defined in terms of the evolved spectrum

$$\sigma^2_{k_{\rm nl}} = \int_0^{k_{\rm nl}} {\rm d}^3 k P(k) = 1, \tag{6}$$

[6]Note that for arguments $x > 1$, one can use the relation $i \arccos x = \ln\left(x + \sqrt{x^2 - 1}\right)$ to recover an explicitly real–valued expression.

is equal to eight in units of the fundamental mode of the simulation box. By using the stage $k_{\rm nl} = 8$, we make sure that structure is already sufficiently developed on scales much larger than the simulation's resolution, while it is not yet influenced by boundary effects.

Using a cloud–in–cell kernel, these particles were put onto a 256^3 grid, which is the maximum value an ordinary workstation can tackle with acceptable time and memory consumption. Subsequently, the density field was smoothed with a Gaussian kernel $\propto \exp\left(-x^2/2\lambda^2\right)$, where x is the distance in mesh units and the width λ is set to 3. Tests have shown that this value both leads to a reasonably smooth field, and preserves at least some detail on smaller scales. Throughout the article, we re–scale the density to the density contrast δ, ranging from -1 to infinity with zero mean.

3.2. The global field

The global Minkowski functionals calculated from the density fields described in the previous section are shown in Figure 2. The four different line styles correspond to the different spectral indices. Figure 3 shows the Minkowski functionals for the same set of models, but instead of the density threshold δ, the rescaled threshold ν is used as the x–axis. ν is calculated from the volume Minkowski functional v_0, that is the filling factor f, as described by Gott III et al. (1987). Essentially, its use forces exact Gaussian behavior of the volume v_0, by the implicit connection

$$v_0(\delta) = \frac{1}{2} - \frac{1}{2}\Phi\left(\frac{\nu}{\sqrt{2}}\right). \tag{7}$$

Thus the deviations from Gaussianity that are due to changes in the one–point probability distribution function are removed, and deviations due to higher–order correlations are emphasized.

Obviously, the global functionals clearly discriminate between the various models. However, in order to make this statement more quantitative, let us take a closer look at the individual coherent objects composing the isodensity contours.

3.3. The largest objects

At intermediate thresholds, the excursion sets consist of numerous isolated objects. We identify them by grouping adjacent occupied grid cells into one object, where adjacent means that the cells have a common face. Since the Minkowski functionals of the global field are

calculated by integrating over quantities that can be assigned to individual grid cells, the partial Minkowski functionals of each object can be obtained at no extra cost once the cells belonging to each object have been identified.

Several plots in Figures 4, 5, 6, and 7 illustrate the behavior of the Minkowski functionals of these objects.

Obviously, the contribution of smaller objects to the volume is almost negligible compared to the largest one. Note that in all figures, the mean and standard deviation over all four realizations are shown instead of the individual curves. It is worth noting that the variance is largest in the $n = -2$ and -1 models, which are dominated by structures on large scales and hence show the strongest sample variance.

The models with various initial spectral indices n show qualitatively a similar behavior. At small filling factors (high density thresholds) the two largest clusters give negligible contribution to each of the global characteristics. Then, at percolation transition the largest cluster quickly becomes the dominant structure in terms of volume, area, and integrated mean curvature. The second largest cluster also grows at the percolation threshold but just a little and then quickly diminishes. The percolation transition is clearly marked in all three characteristics of the largest cluster by their sudden growth. However, this transition does not happen at a well–defined threshold. Instead, clusters gradually merge into the largest objects as the threshold is decreased (the filling factor grows). This continuous transition has also been observed using percolation analysis, i.e. the zeroth Minkowski functional alone (Shandarin & Zel'dovich 1983; Shandarin & Yess 1998; Klypin & Shandarin 1993; Sahni et al. 1997) and is explained by the finite size of the sample.

Nevertheless, the percolation transitions happen within fairly narrow ranges of the filling factor that are clearly distinct for different models in question: The filling factors are approximately $0.03 \pm 0.01, 0.07 \pm 0.015, 0.11 \pm 0.015, 0.14 \pm 0.015$ in the $n = -2, -1, 0, +1$ models, respectively. It is remarkable that all percolation transitions occur at smaller filling factors than in Gaussian fields (about 0.16) indicating that even in the most hierarchical model ($n = +1$) the structures tend to be more connected than in the "structureless" Gaussian field. Pauls & Melott (1995) showed positive correlation with networks based on the same phases all the way to $n = +3$. This confirms the conclusion of Yess & Shandarin (1996): The universality of the network structures results from the evolution of Gaussian initial conditions through gravitational instability. The Euler characteristic of the largest cluster also marks the percolation threshold but in a different manner: before percolation it is zero and after percolation it becomes negative in every model, however, in the $n = 0$ and $n = +1$ models it grows to a small positive peak before becoming negative. All global functionals have no particular features at the percolation threshold.

3.4. Small objects

As an example, the Blaschke diagram for the model $n = -2$ is shown in Figure 8. The distributions for the other models look qualitatively very similar and the average quantities for other models are presented in Figures 9 and 10. Figure 9 shows that most of the small objects are either spherical or slightly planar (two largest dots in Figure 8). There is also a considerable number of elongated clusters with filamentarities from 0.1 to 0.5. In some cases filamentarity reaches large values ~ 1. On the contrary planarity is much weaker, it hardly reaches the value of 0.2 (which is partly a consequence of the smoothing). There is a hint of a small correlation between filamentarity and planarity: the objects with the largest filamentarity also tend to have larger planarity.

Figures 9 and 10 display the shapefinders as functions of the cluster mass. The curves give averages over the realizations of each model. Apparently, the signal for filamentarity is much stronger than for planarity, regardless of the model which is in full agreement with Figure 8. The planarity and filamentarity distributions qualitatively look very similar except the amplitude. Small objects ($5 \times 10^{-6} \lesssim m \lesssim 5 \times 10^{-4}$) display stronger planarity and filamentarity for models with more power on large scales. However, for greater masses ($m \gtrsim 5 \times 10^{-4}$) the situation is reversed: the less large-scale power the greater the filamentarity and planarity. If the former seems to be natural and was expected, the latter has been unexpected. Both the planarity and filamentarity monotonically grow and reach their maxima at largest clusters: $\mathcal{P}_m \approx 0.1$ and $\mathcal{P}_m \approx 0.5$ in all models. As expected the largest objects possess the largest planarities and filamentarities, but the independence of the maxima from the model again was unexpected. Figures 11 and 12 show the histograms for the shapefinders $\mathcal{P}$ and $\mathcal{F}$, respectively. They clearly show the large difference in the total number of structures: the more power on small scales the greater the abundance of clusters. These figures are in general agreement with the Figures 9 and 10.

4. Conclusion and Outlook

Global Minkowski functionals do discriminate (Figures 2 and 3). Only the $n = -2$ model shows slight drawbacks as far as robustness is concerned, but that is due to the method's sensitivity to large–scale features of the smoothed density field. The total area, mean curvature, and Euler characteristic are sensitive to abundances of the structures and are easy to interpret: the more power on small scales (greater n) the more abundant structures and therefore the greater the amplitude of the curve.

Even more valuable information is obtained from looking at the Minkowski functionals

of the largest coherent object at each threshold (Figures 4, 5, 6, and 7). All four Minkowski functionals of the largest cluster clearly consistently detect the percolation transition. Two points are worth stressing: 1) in all models the percolation transition happens at smaller filling factors than in the "structureless" Gaussian fields and 2) the more power on the large scales (i.e. the smaller n) the smaller the filling factor at percolation. Both conclusions confirm the results of Yess & Shandarin (1996) about the universality of the network structures in the power law models with $n \leq 1$. The results of Pauls & Melott (1995) present evidence that this should be expected all the way up to $n = +3$; at $n = +4$ mode coupling effects from smaller scales should begin to fully disrupt the network structure.

Small objects, on the other hand, give different results. Their abundance discriminates well, but is already determined by the difference in the Euler characteristic as well as by the total area and mean curvature of the whole contour (Figures 2 and 3) that are also sensitive to the abundance of structures. The morphology of small objects as measured by shapefinders shows little differences between models so far (Figures 9, 10, 11 and 12). Both the maximum average planarity ($\mathcal{P} \approx 0.1$) and the maximum average filamentarity ($\mathcal{F} \approx 0.5$) are reached in the most massive non-percolating objects. None of the model showed ribbon–like objects characterized by both large planarity and large filamentarity. We may speculate that the smaller objects are ones which formed earlier, are more nonlinear, and therefore more decoupled from initial conditions.

However, all models used Gaussian initial conditions, and evolve under the influence of gravity. Hence the similar morphology of the clumps may point towards universal behavior. Note that things such as string wakes might produce totally different results.

The grouping and measurement techniques used in this study may be less accurate for small objects than for large clusters. It is worth trying to study the morphology of small objects by applying more accurate methods of measuring partial Minkowski functionals such as a Boolean grain model (Schmalzing 1996, and a follow–up to this article) or the interpolation method of Novikov et al. (1998) generalized to three dimensions.

Acknowledgments

JS wishes to thank Martin Kerscher for interesting discussions and valuable comments. This work is part of a project in the "Sonderforschungsbereich 375–95 für Astroteilchenphysik" of the Deutsche Forschungsgemeinschaft. ALM and SFS acknowledge support of the NSF–EPSCoR program and the GRF program at the University of Kansas. SFS acknowledges support from TAC in Copenhagen.

A. Calculating Minkowski functionals of isodensity contours

Using methods from integral geometry and scale–space theory, Schmalzing & Buchert (1997) developed numerical methods to quantify the morphology of isodensity contours of a random field. They present two complementary possibilities for estimating Minkowski functionals.

Given a density field sampled at the grid points of a cubic lattice with lattice constant a, Crofton's formula (Crofton 1868) requires counting of the number of grid cells per unit volume contained in the excursion set. We obtain

$$\widehat{V}_0(\nu) = n_3, \tag{A1}$$
$$\widehat{V}_1(\nu) = \tfrac{2}{9a}(n_2 - 3n_3), \tag{A2}$$
$$\widehat{V}_2(\nu) = \tfrac{2}{9a^2}(n_1 - 2n_2 + 3n_3), \tag{A3}$$
$$\widehat{V}_3(\nu) = \tfrac{1}{a^3}(n_0 - n_1 + n_2 - n_3), \tag{A4}$$

where the quantity n_j is the number density of j–dimensional elementary cells; to be specific, n_3 is the number of grid volumes, n_2 counts the grid faces, and n_1 and n_0 denote the numbers of grid edges and lattice points, respectively.

Alternatively, it is sufficient to estimate the derivatives of the random field at the grid points and perform a spatial average $\langle\cdot\rangle_{\mathcal{D}} = \frac{1}{\mathcal{D}}\int\limits_{\mathcal{D}} \mathrm{d}^3x\cdot$ over Koenderink invariants[7]

$$\widehat{V}_0(\nu) = \langle\Theta(u-\nu)\rangle_{\mathcal{D}}\,, \tag{A5}$$
$$\widehat{V}_1(\nu) = \left\langle \tfrac{1}{6}\delta(u-\nu)(u_{,i}u_{,i})^{1/2}\right\rangle_{\mathcal{D}}\,, \tag{A6}$$
$$\widehat{V}_2(\nu) = \left\langle \tfrac{1}{3\pi}\delta(u-\nu)\tfrac{\epsilon_{ijm}\epsilon_{klm}u_{,i}u_{,jk}u_{,l}}{2u_{,n}u_{,n}}\right\rangle_{\mathcal{D}}\,, \tag{A7}$$
$$\widehat{V}_3(\nu) = \left\langle \tfrac{1}{4\pi}\delta(u-\nu)\tfrac{\epsilon_{ijk}\epsilon_{lmn}u_{,i}u_{,l}u_{,jm}u_{,kn}}{2(u_{,p}u_{,p})^{3/2}}\right\rangle_{\mathcal{D}}\,. \tag{A8}$$

Careful analysis reveals that both families of estimators are biased by the finite lattice constant a encountered with any practical realization of a random field. The deviations are of order a^2 and can be evaluated analytically for a Gaussian random field (see Winitzki & Kosowsky 1997 for some results). It turns out that the two estimates using Crofton's formula and Koenderink invariants, respectively, deviate from the true value in opposite directions.

[7]The notation is chosen to emphasize the coordinate invariance of the integrand. We use indices following a comma to indicate differentiation with respect to the corresponding coordinate. ϵ_{ijk} denotes the components of the totally antisymmetric third–rank tensor normalized to $\epsilon_{123} = 1$. Summation over pairwise indices is understood.

Hence their difference gives at least a rough idea of the errors associated with binning the continuous field onto a finite lattice.

Yet another method of calculating Minkowski functionals of isocontours was suggested by Novikov et al. (1998). However, their interpolation method has so far only been implemented in two dimensions.

B. Isoperimetric inequalities and shapefinders

In his original article, Minkowski (1903) introduced the mixed volumes $V(K_1, \ldots, K_n)$ of n convex bodies K_1 to K_n. In terms of ordinary volumes of Minkowski sums of the bodies, we have

$$V(K_1, \ldots, K_n) := \frac{1}{n!} \sum_{k=1}^{n} (-1)^{n+k} \sum_{i_1 < \ldots < i_k} V(K_{i_1} \oplus \ldots \oplus K_{i_k}), \tag{B1}$$

where the Minkowski sum is defined as

$$K \oplus L := \{x + y | x \in K, y \in L\}\,. \tag{B2}$$

In the case of a single body, the mixed volume reduces to its ordinary volume. Furthermore, these quantities inherit many interesting properties from the volume and hence play a central role in the Brunn–Minkowski theory (see Schneider 1993 for an introduction).

A most useful inequality proved by Alexandrov (1937) and Fenchel (1936) states that

$$V^2(K_1, K_2, \ldots, K_n) \geq V(K_1, K_1, K_3 \ldots, K_n)\, V(K_2, K_2, K_3 \ldots, K_n). \tag{B3}$$

The Minkowski functionals of a body K in d dimensions can be related to mixed volumes of two bodies via[8]

$$V_j(K) = \frac{1}{\omega_j} V(\underbrace{K, \ldots, K}_{d-j}, \underbrace{B, \ldots, B}_{j}), \tag{B4}$$

[8]The volume of the j–dimensional unit ball is denoted by ω_j. Some special values are $\omega_0 = 1$, $\omega_1 = 2$, $\omega_2 = \pi$, and $\omega_3 = \frac{4\pi}{3}$. The general formula reads

$$\omega_j = \frac{\pi^{j/2}}{\Gamma\left(j/2 + 1\right)}.$$

where B denotes the d–dimensional unit ball. Consult the book by Burago & Zalgaller (1988) for a broad discussion of the Alexandrov–Fenchel inequality and related issues.

In three dimensions, the Alexandrov–Fenchel inequality (B3) leads to two independent non–trivial inequalities for the Minkowski functionals, namely

$$V_1{}^2 \geq \tfrac{\pi}{4} V_0 V_2, \tag{B5}$$

$$V_2{}^2 \geq \tfrac{8}{3\pi} V_1 V_3. \tag{B6}$$

$$\tag{B7}$$

These two inequalities motivate the introduction of the Blaschke diagram (Hadwiger 1955). A convex body with Minkowski functionals V_j is mapped to a point (x, y) with coordinates

$$x := \frac{\pi V_0 V_2}{4 V_1^2}, \qquad y := \frac{8 V_1 V_3}{3\pi V_2^2}. \tag{B8}$$

A ball has $x = y = 1$. For convex bodies, all Minkowski functionals are non–negative, and satisfy the inequalities (B5), so these points are confined to the unit square. Nevertheless, the convex bodies do not fill the whole unit square – the limiting isoperimetric inequality has yet to be found (Schneider 1993 and references therein).

The dimensionless shapefinders introduced in equation (2) are related to the isoperimetric ratios via

$$\mathcal{P} = \frac{1-x}{1+x}, \qquad \mathcal{F} = \frac{1-y}{1+y}. \tag{B9}$$

Obviously, a scatter plot of shapefinders is almost equivalent to the ordinary Blaschke diagram reflected at the point $(0.5, 0.5)$, so either method of presentation should convey the same morphological information. Throughout this article, we refer to plots of shapefinders $(\mathcal{P}, \mathcal{F})$ as Blaschke diagrams.

REFERENCES

Alexandrov, A. D., Matem. Sb. SSSR **2** (1937), 1205–1238, in Russian, summary in German.

Babul, A. & Starkman, G. D., ApJ **401** (1992), 28–39.

Barrow, J. D., Sonoda, D. H., & Bhavsar, S. P., MNRAS **216** (1985), 17–35.

Bond, J. R., Kofman, L., & Pogosyan, D. Yu., Nature **380** (1996), 603–605.

Burago, Yu. D. & Zalgaller, V. A., *Geometric inequalities*, Springer Verlag, Berlin, 1988.

Crofton, M. W., Phil. Trans. Roy. Soc. London **158** (1868), 181–199.

Fenchel, D., C. R. Acad. Sci. Paris **203** (1936), 647–650, in French.

Gott III, J. R., Melott, A. L., & Dickinson, M., ApJ **306** (1986), 341–357.

Gott III, J. R., Weinberg, D. H., & Melott, A. L., ApJ **319** (1987), 1–8.

Hadwiger, H., *Altes und Neues über konvexe Körper*, Birkhäuser, Basel, 1955.

Hadwiger, H., *Vorlesungen über Inhalt, Oberfläche und Isoperimetrie*, Springer Verlag, Berlin, 1957.

Klypin, A. & Shandarin, S. F., ApJ **413** (1993), 48–58.

Luo, S. & Vishniac, E., ApJS **96** (1995), 001–005.

Mecke, K. R., Buchert, T., & Wagner, H., Astron. Astrophys. **288** (1994), 697–704.

Melott, A. L. & Shandarin, S. F., ApJ **410** (1993), 469–481.

Melott, A. L., Einasto, J., Saar, E., Suisalu, I., Klypin, A. A., & Shandarin, S. F., Phys. Rev. Lett. **51** (1983), 935–938.

Minkowski, H., Mathematische Annalen **57** (1903), 447–495, in German.

Mo, H. & Buchert, T., Astron. Astrophys. **234** (1990), 5–19.

Novikov, D., Feldman, H. A., & Shandarin, S. F., ApJ (1998), submitted, astro-ph/9809238.

Pauls, J. L. & Melott, A. L., MNRAS **274** (1995), 99–109.

Peebles, P., Astron. Astrophys. **32** (1974), 197–202.

Sahni, V. & Coles, P., Physics Rep. **262** (1995), 1–135.

Sahni, V., Sathyaprakash, B. S., & Shandarin, S. F., ApJ **476** (1997), L1–L5.

Sahni, V., Sathyaprakash, B. S., & Shandarin, S. F., ApJ **495** (1998), L5–L8.

Sathyaprakash, B. S., Sahni, V., & Shandarin, S. F., ApJ **508** (1998), 551–569.

Schmalzing, J. & Buchert, T., ApJ **482** (1997), L1–L4.

Schmalzing, J., Diplomarbeit, Ludwig–Maximilians–Universität München, 1996, in German, English excerpts available.

Schneider, R., *Convex bodies: the Brunn–Minkowski theory*, Cambridge University Press, Cambridge, 1993.

Shandarin, S. F. & Yess, C., ApJ **505** (1998), 12.

Shandarin, S. F. & Zel'dovich, Ya. B., Comments Astrophys. **10** (1983), 33–45.

Shandarin, S. F., Sov. Astron. Lett. **9** (1983), 104–106.

Totsuji, H. & Kihara, T., PASJ **21** (1969), 221.

Winitzki, S. & Kosowsky, A., New Astronomy **3** (1997), 75–100.

Yess, C. & Shandarin, S. F., ApJ **465** (1996), 2–13.

Zel'dovich, Ya. B. & Shandarin, S. F., Sov. Astron. Lett. **8 (3)** (1982), 139–140.

	geometric quantity	μ	V_μ
V	volume	0	$V_0 = V$
A	surface	1	$V_1 = A/6$
H	mean curvature	2	$V_2 = H/3\pi$
χ	Euler characteristic	3	$V_3 = \chi$

Table 1: Minkowski functionals expressed in terms of the corresponding geometric quantities.

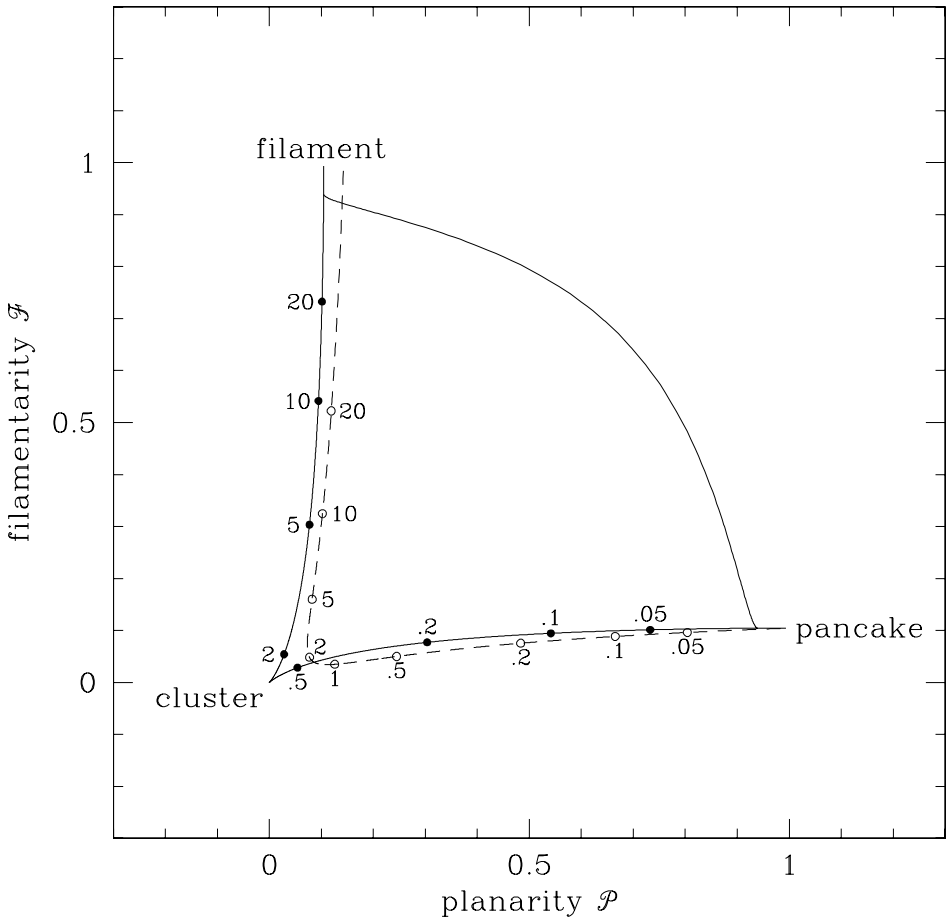

Fig. 1.— The shapefinders of some convex bodies. The solid line shows the transition from a ball to a filament to a pancake and back to a ball via triaxial ellipsoids of various shapes. The dashed line corresponds to cylinders that also undergo the transition from a filament to a pancake by varying their height. The dots on the spheroid and cylinder curves indicate typical values of the λ parameter from Equations (3) and (5), respectively.

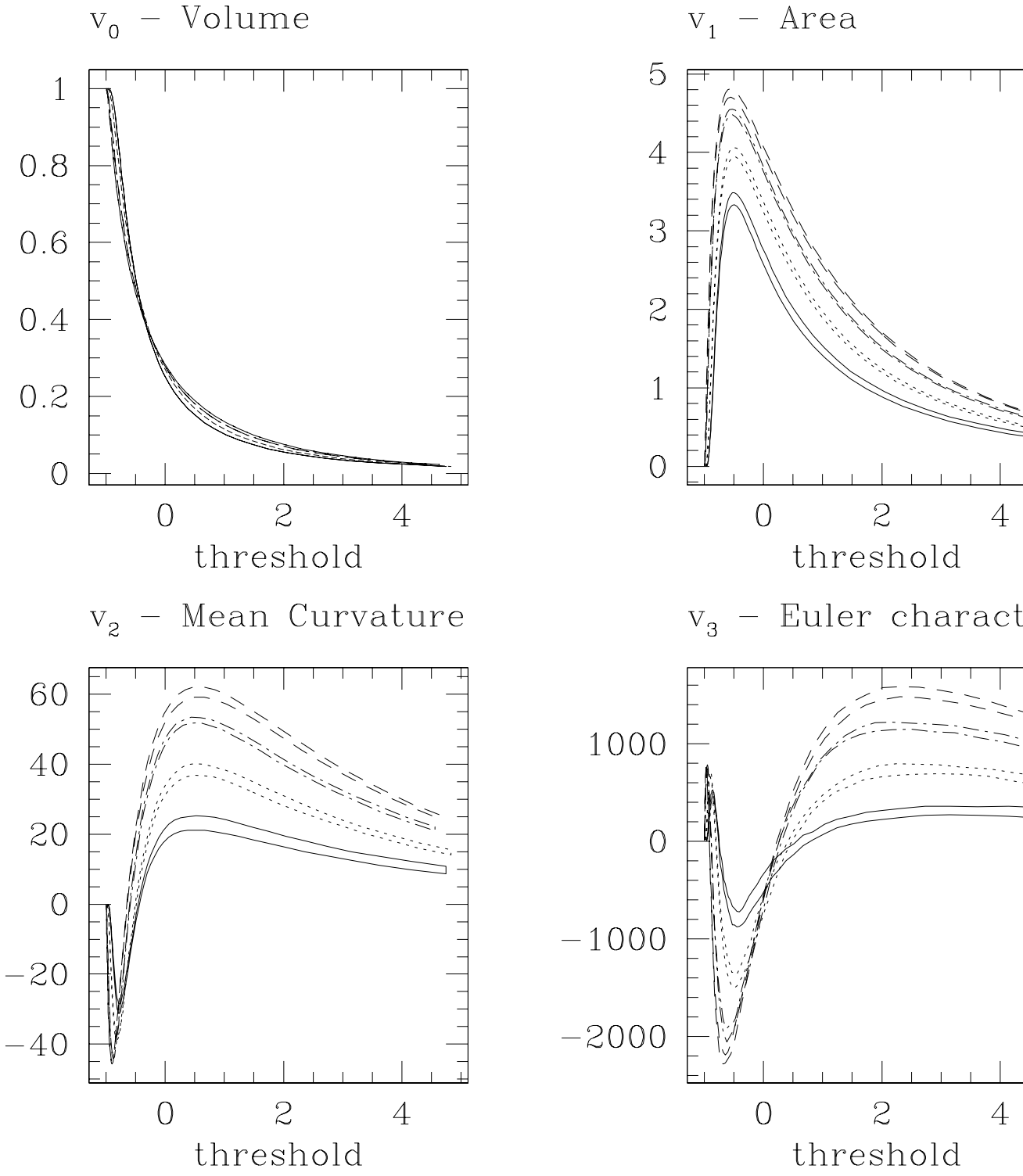

Fig. 2.— Minkowski functionals for the evolutionary stage $k_{\rm nl} = 8$ of four different models with initial power law spectra $P(k) \propto k^n$. The area between two lines gives the one–sigma deviations of four realizations from their mean. The solid lines correspond to $n = -2$, dotted is $n = -1$, dash–dotted lines give the results for $n = 0$, and $n = +1$ is shown with dashed lines.

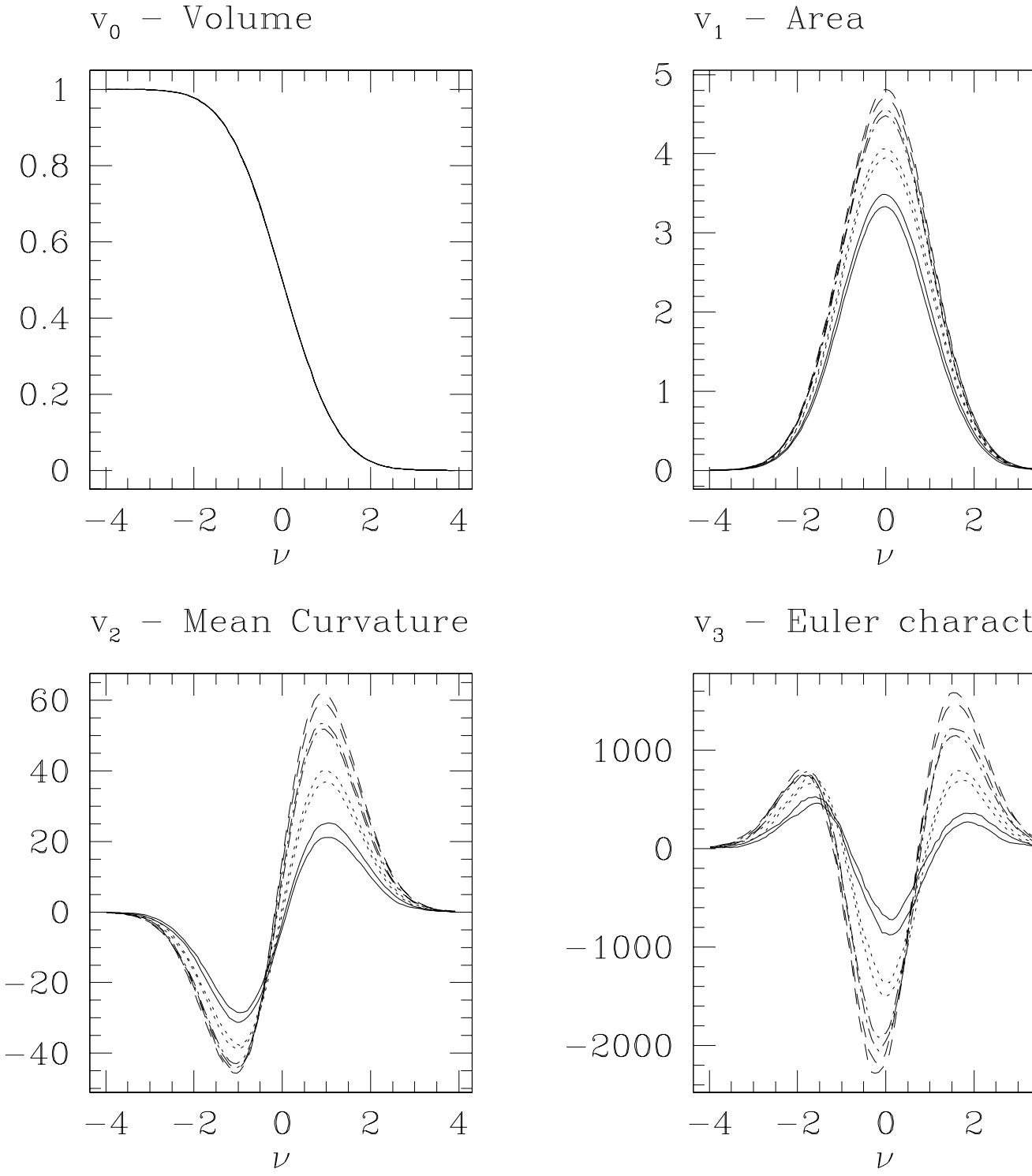

Fig. 3.— Minkowski functionals for the evolutionary stage $k_{\rm nl} = 8$ of four different models with initial power law spectra. Line styles are the same as in the previous figure, but instead of the density threshold δ, the rescaled threshold ν introduced by Gott III et al. (1987) is used.

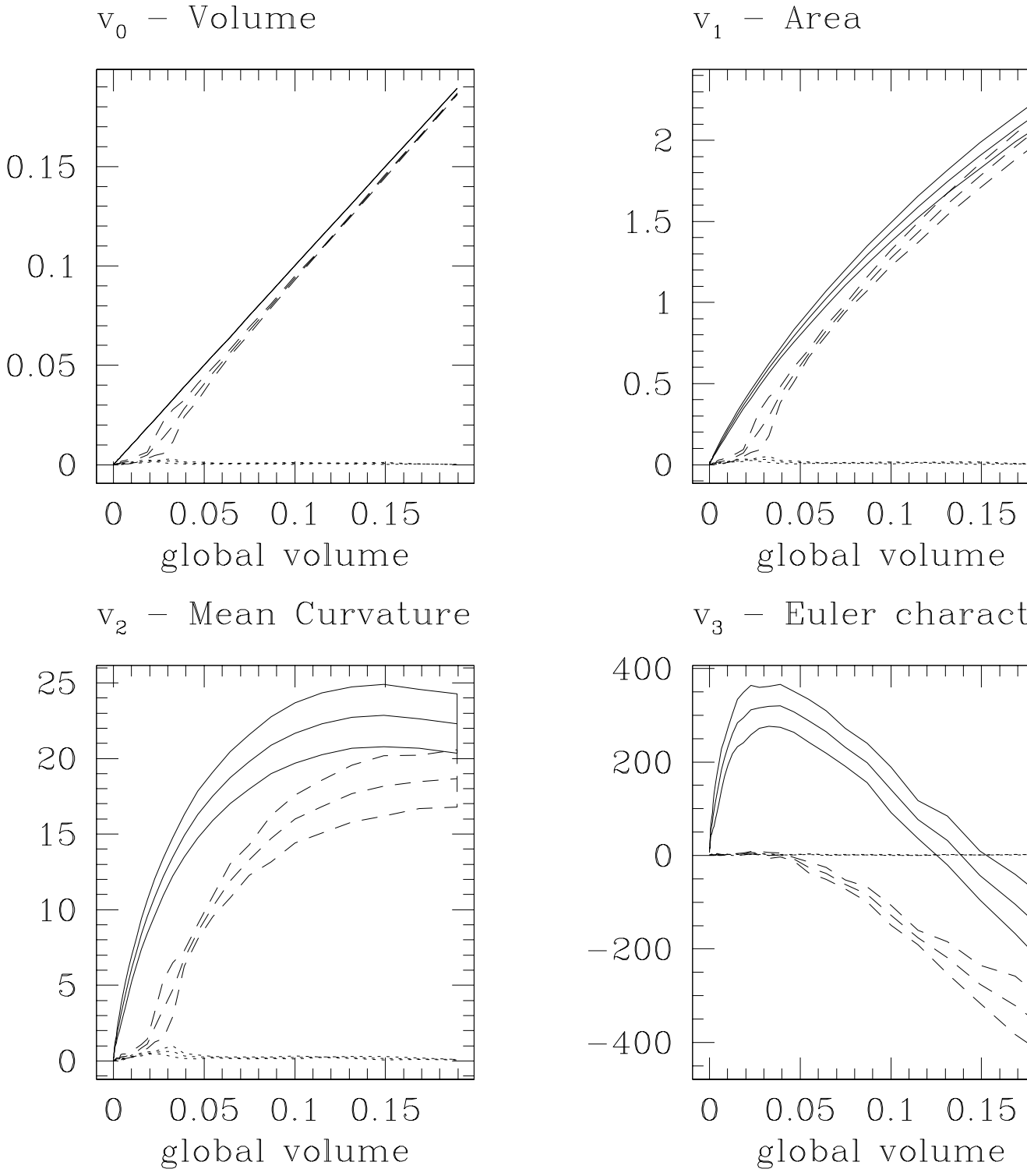

Fig. 4.— The following set of figures compares the global Minkowski functionals of the whole density field (solid line) to the Minkowski functionals of the largest (dashed) and second largest (dotted) objects. The areas indicate the mean and standard deviation over the four realizations of each model. In order to emphasize the region around the percolation transition, the Minkowski functionals are plotted against the filling factor, which is equal to the volume enclosed in all isocontours of the global field. In this particular plot, the values

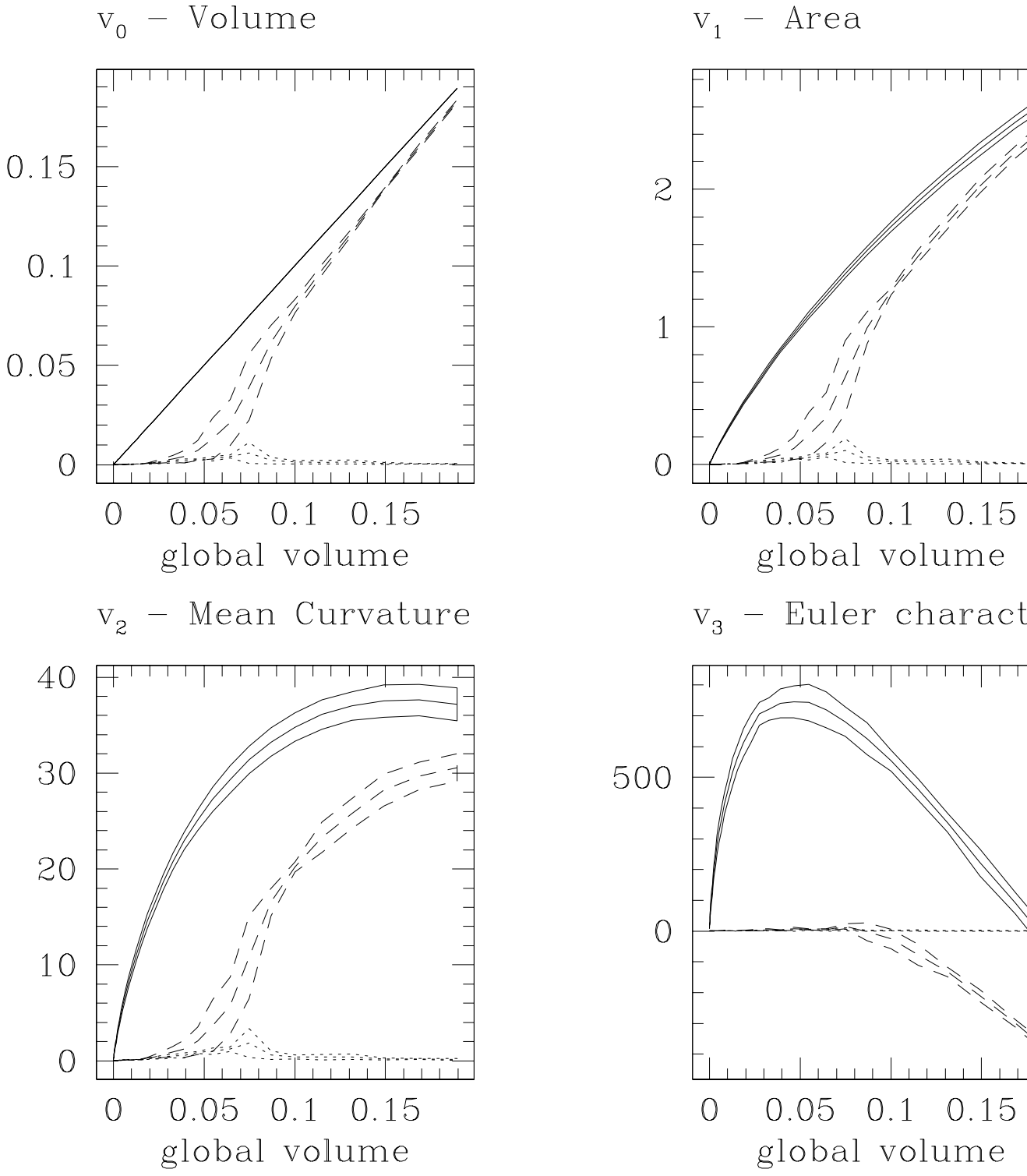

Fig. 5.— The same tendency as before is visible in this case where $n = -1$. As before, the dominance of large networked structures is clearly visible – for example, the Euler characteristic stays well below zero even for high thresholds, which indicates a spongy structure with many tunnels in it. However, the networked structures have fewer loops, since they tend to split up at lower thresholds.

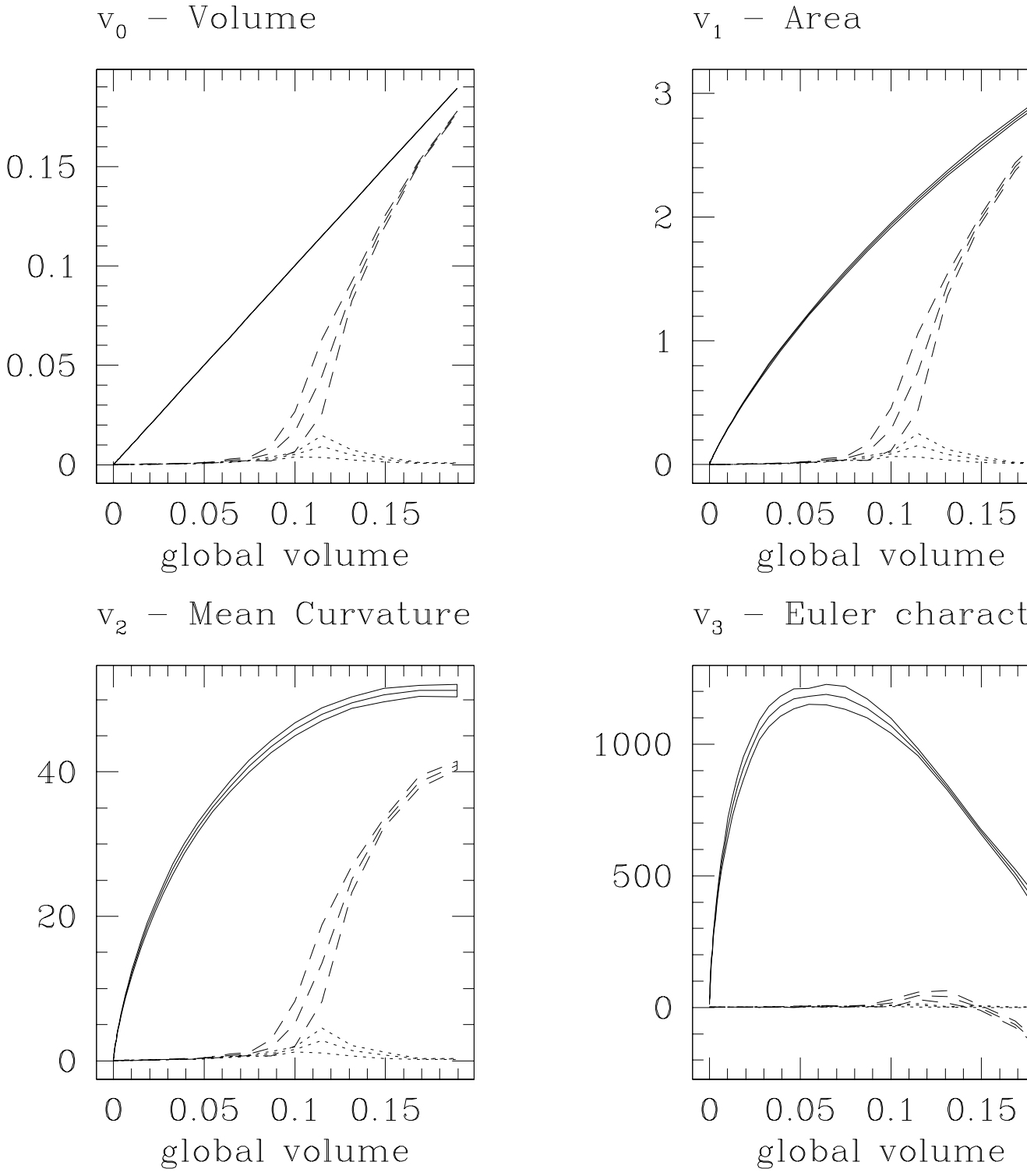

Fig. 6.— The situation is different in the case $n = 0$. The largest object splits up rapidly, and is already simply connected at fairly low density contrast ($\delta \approx 0.5$). Also, at thresholds around percolation, the second largest object becomes comparable to the largest one, so the field is not dominated by a single networked structure, but by several chunks.

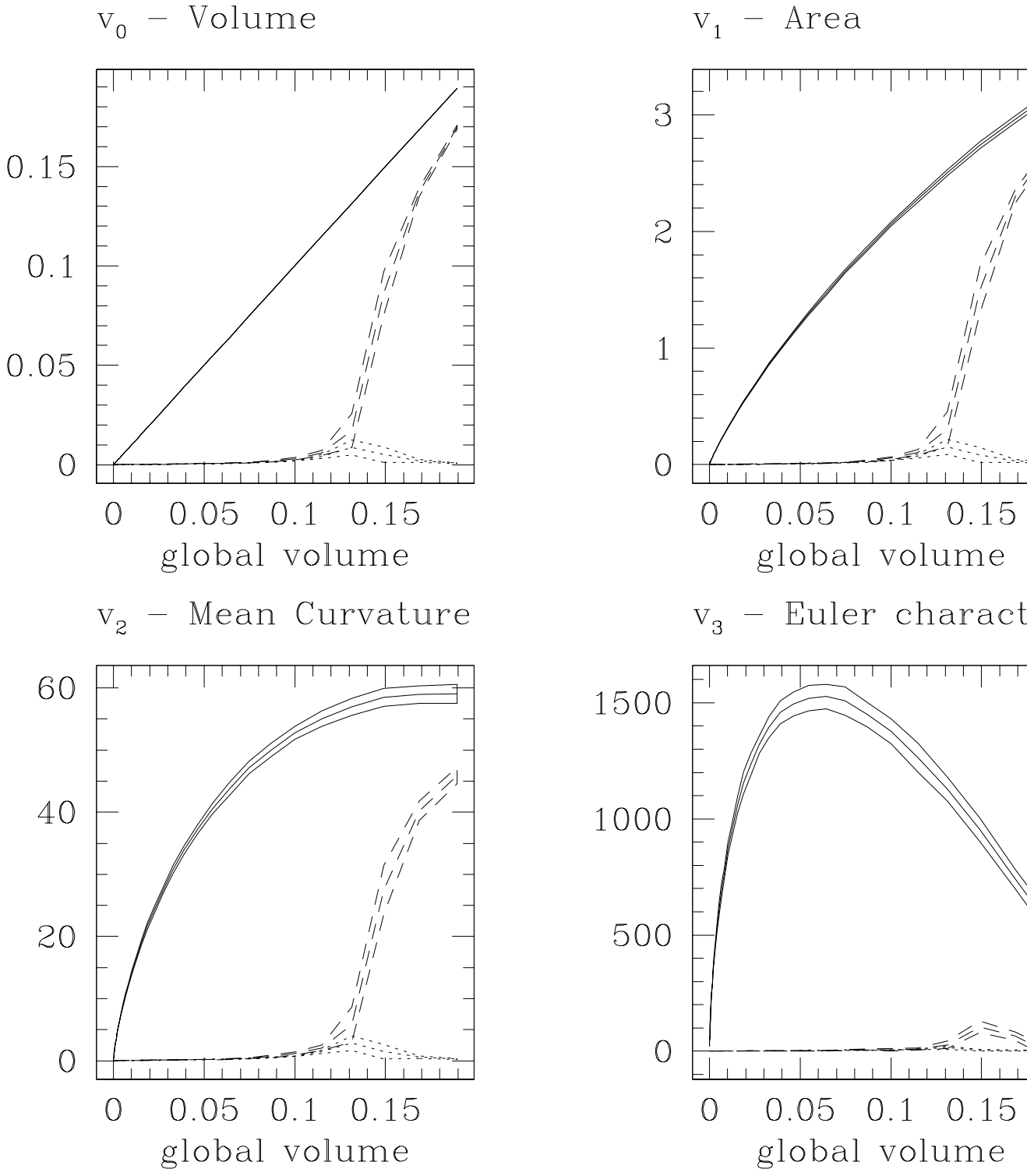

Fig. 7.— The effect described in the previous figure is even more pronounced for $n = +1$, since this model is dominated by small–scale structures. Contrary to the models with negative index n, where the Euler characteristic of the largest object approaches the value one for a simply connected structure from below, one can even see a small positive peak around the percolation threshold.

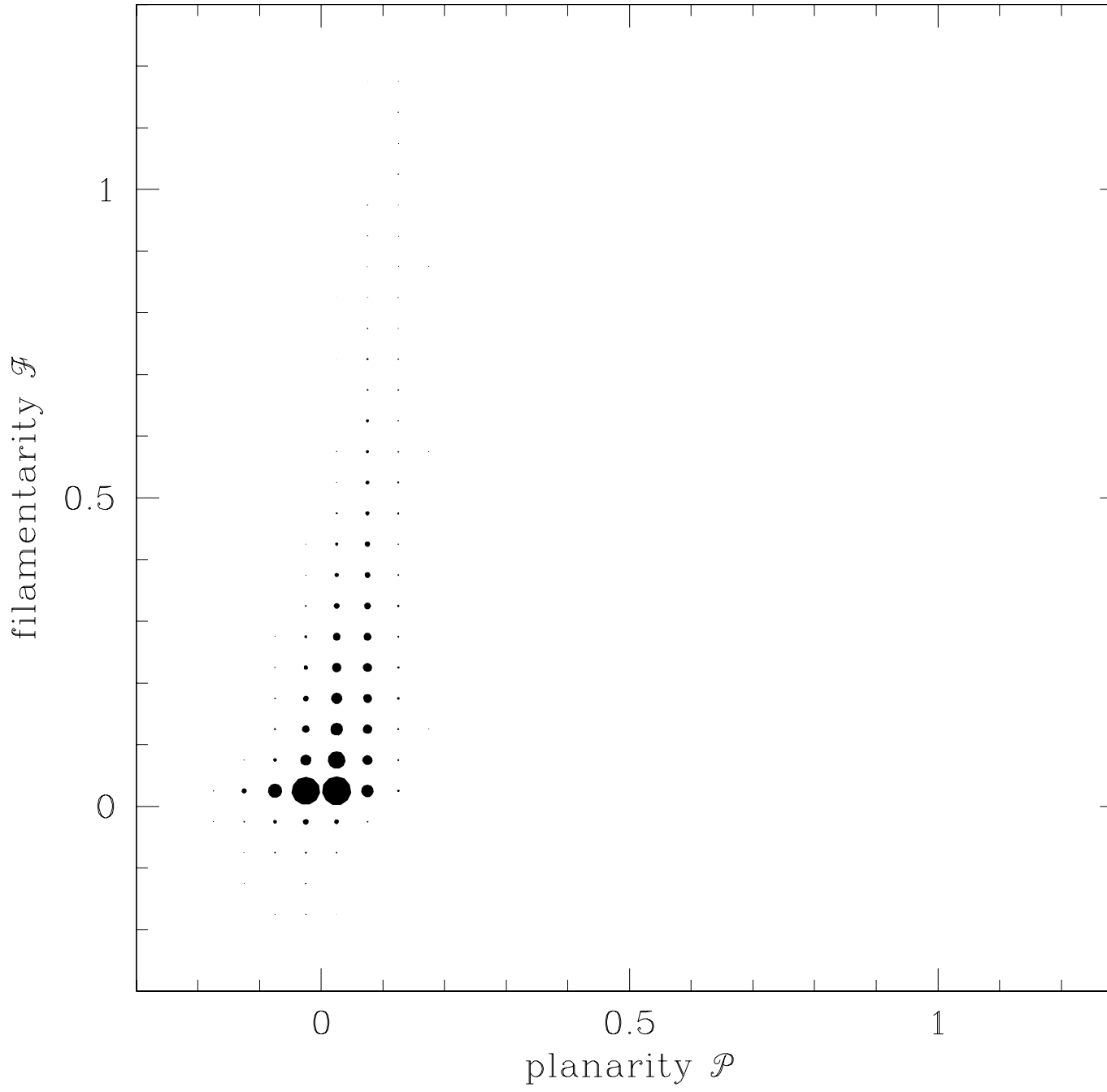

Fig. 8.— The shapefinder or Blaschke diagram of the model with $n = -2$. The area of each dot corresponds to the number of coherent objects whose shapefinders $(\mathcal{P}, \mathcal{F})$ lie around the center of this dot. Note that the shapefinders of all objects at all thresholds are used in the construction of the diagram. Nevertheless, most information comes from thresholds close to percolation, where small objects are abundant.

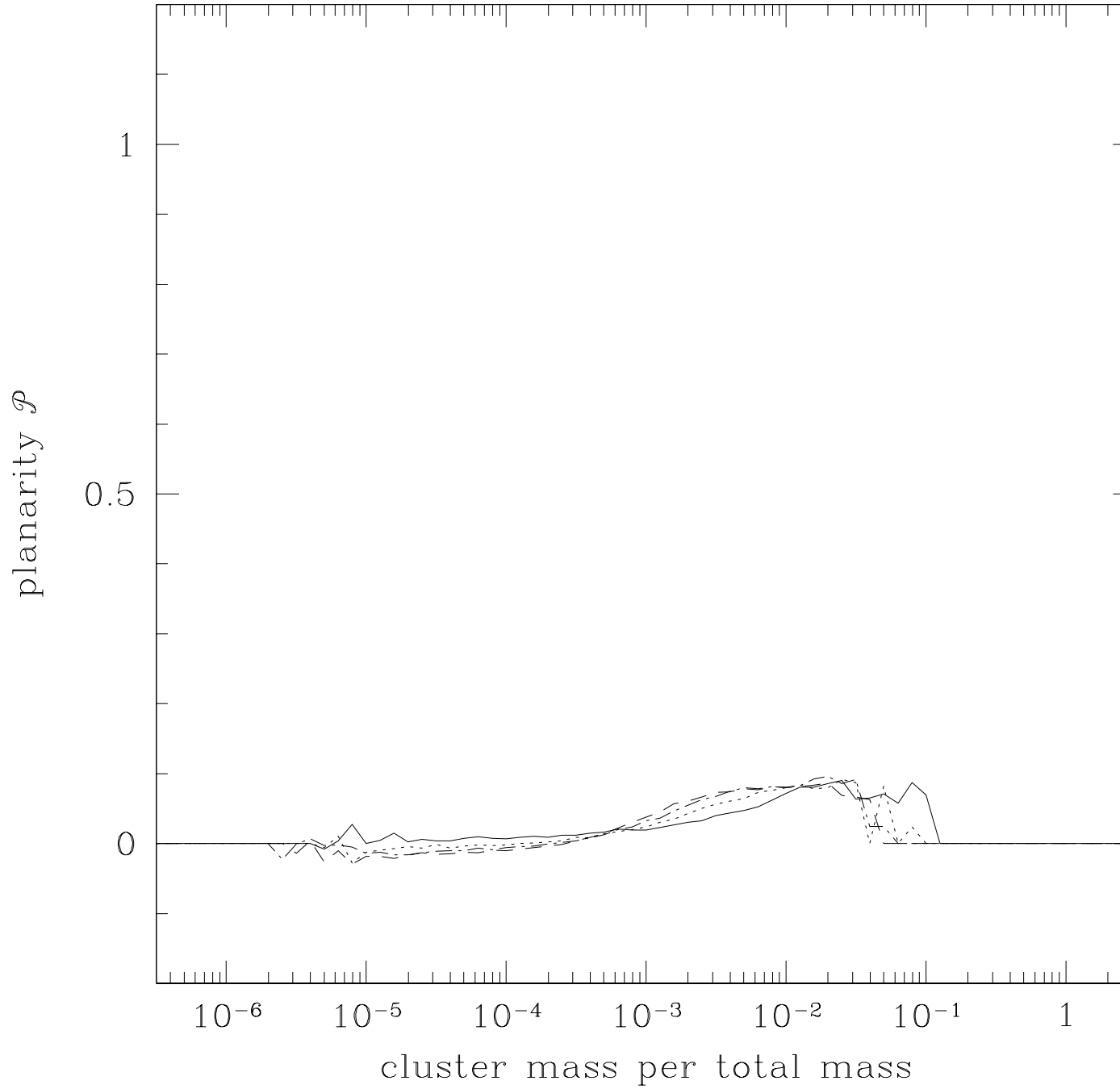

Fig. 9.— The average planarity shapefinder $\mathcal{P}$ as a function of the cluster mass. Line styles are explained in Figure 2. As in Figure 8, all objects at all thresholds are used to improve statistics.

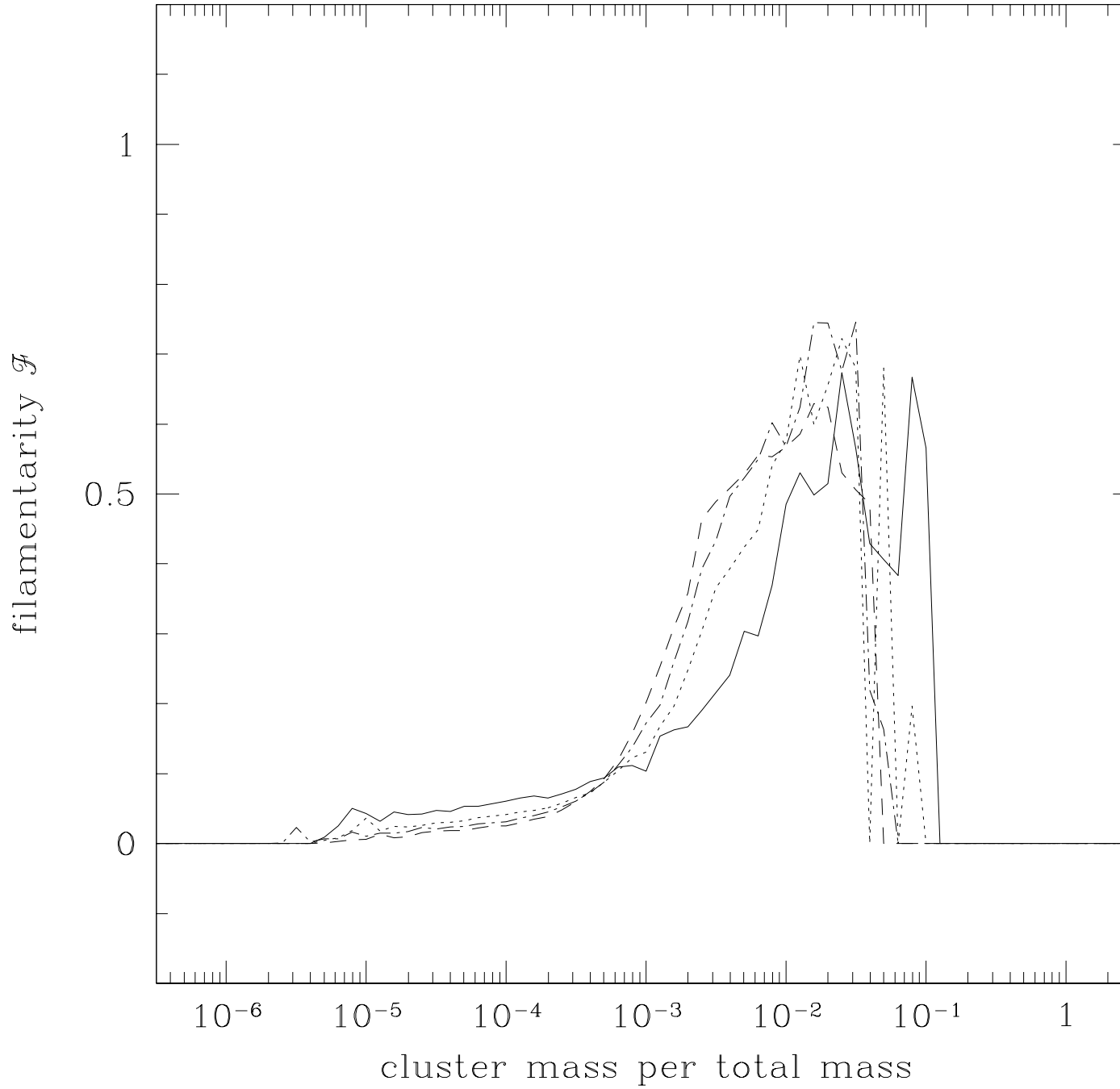

Fig. 10.— This plot shows the same type of distribution as the previous Figure 9, but this time the average filamentarity shapefinder $\mathcal{F}$ is plotted as a function of the cluster mass. Again, line styles correspond to models as explained in the caption of Figure 2.

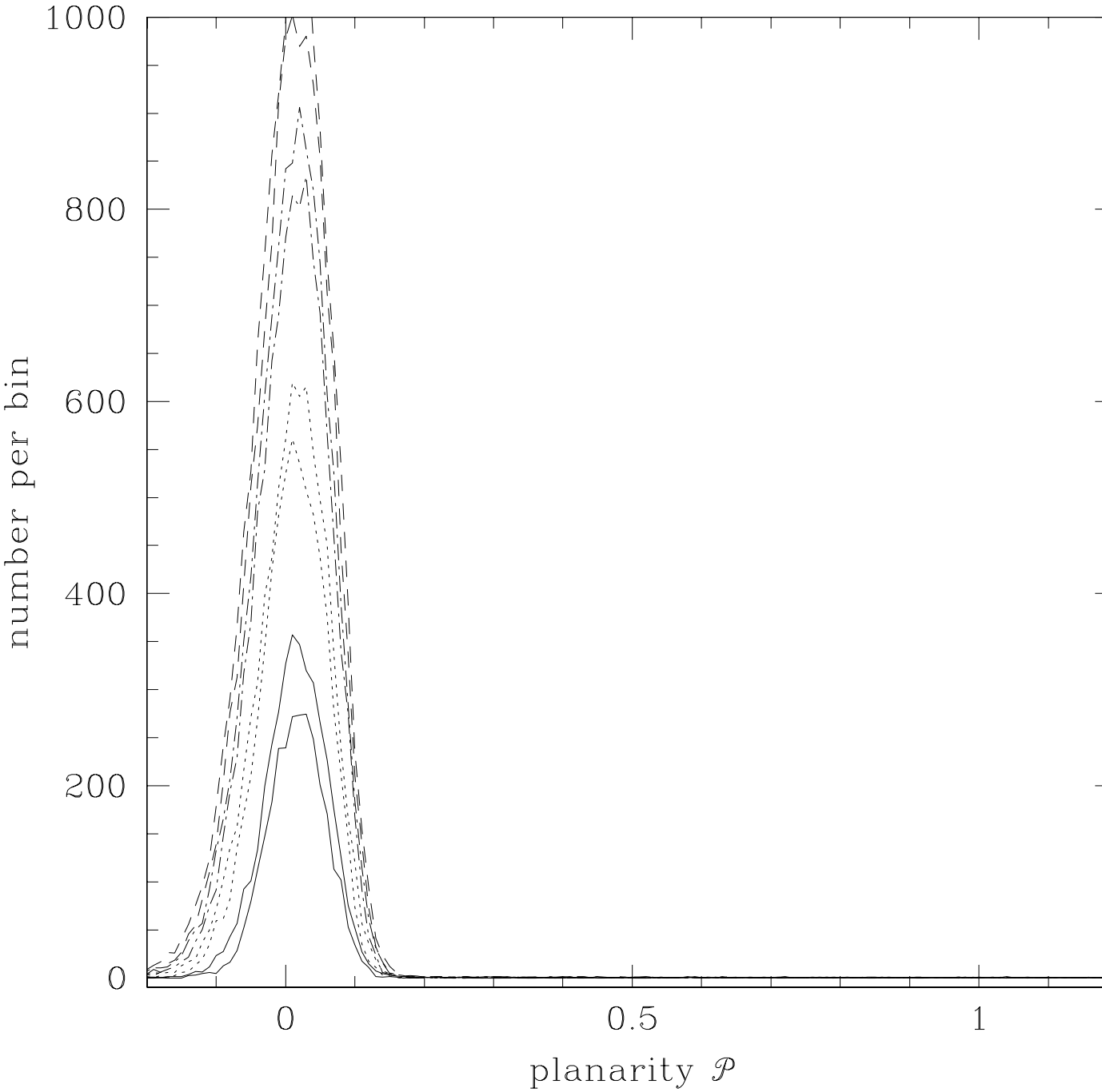

Fig. 11.— The distribution of the planarity shapefinder $\mathcal{P}$. The histogram only includes objects larger than 10^{-5} times the simulation box, a value of the order of the smoothing volume. Note that although theoretically, the value should lie between 0 and 1, measurement errors lead to negative values. The curves give total numbers of objects per histogram interval, hence they differ widely in normalization, but still agree reasonably well in shape. Line styles are explained in Figure 2.

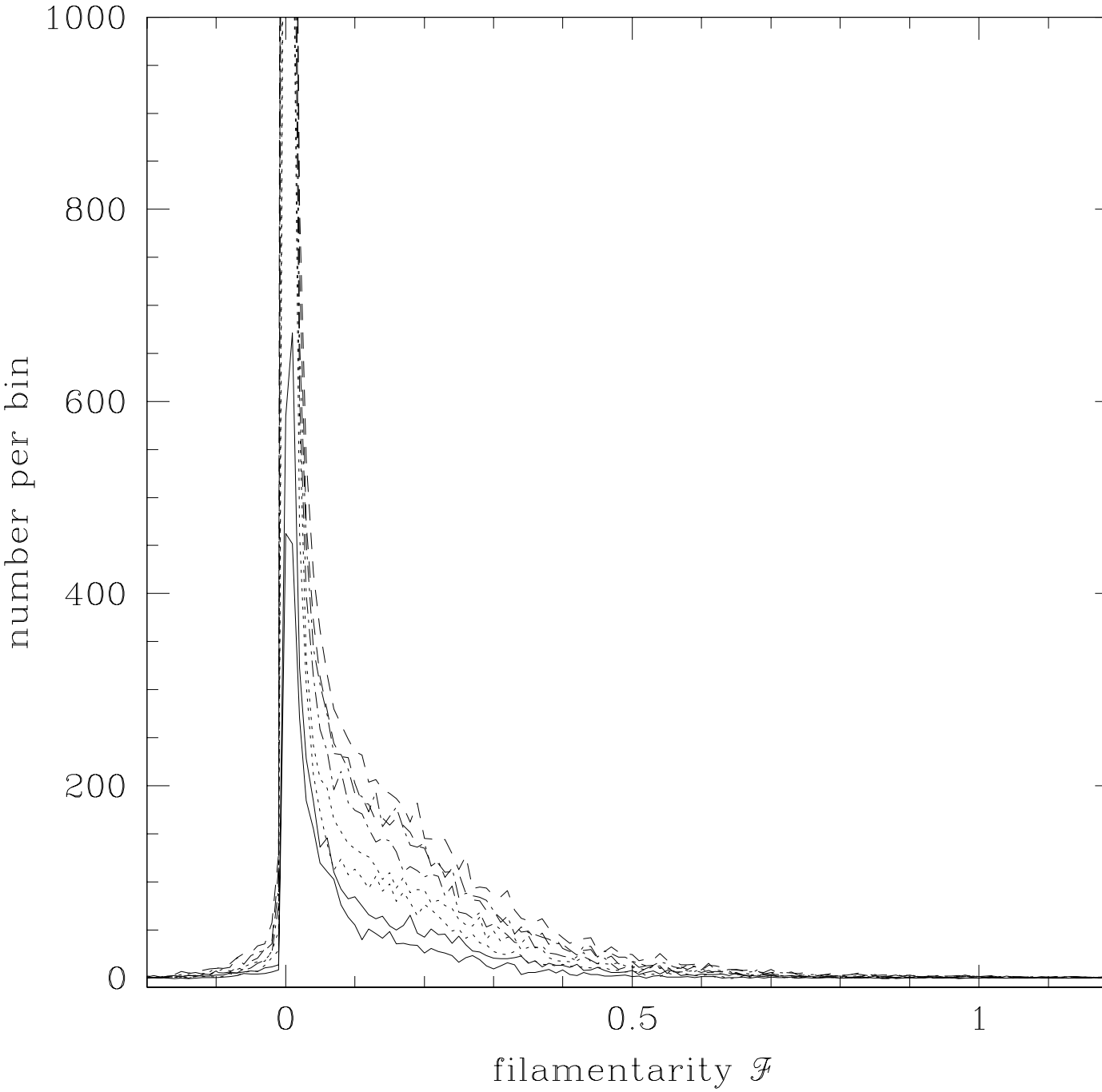

Fig. 12.— This figure displays the same type of distribution as above, but shows the filamentarity shapefinder $\mathcal{F}$. Line styles are explained in Figure 2.